A Study of the Secondary Flow in Aircraft Engine Compressor Disks using Computational Fluid Dynamics

Syed Naveed Ahmed[1], Dr. P Ravinder Reddy[2], Dr Sri Ram Venkatesh[3]

1) *PhD Scholar, Mechanical Engineering Department, Osmania University, Hyderabad, Telangana, India.*
2) *Professor, Head, Mechanical Engineering Department, CBIT, Hyderabad, Telangana, India.*
3) *Professor, Mechanical Engineering Department, Osmania University, Telangana, India*

Abstract

The compressor disks of an aircraft engine which operate at very high rotational speeds are exposed to significant temperature gradients. These temperature gradients induce thermal stresses into the rotating disks which along with the existing dynamic stresses significantly reduce their useful field life. Hence it becomes essential to reduce the disk temperature gradients by utilizing a certain percentage of the compressor core flow known as the secondary flow for either heating or cooling these rotating parts. But this extraction of the compressor core flow results in a higher engine fuel burn for a given engine thrust. Hence the need arises for a better utilization of the secondary flow to effectively reduce the temperature gradients of the rotating compressor disks. As the secondary flow thermal phenomenon inside the rotating compressor disk cavities is very complex and due to it's direct impact on the life expectancy of the disks it becomes critical to understand it's thermo-fluid behaviour by the effective use of available Computational Fluid Dynamic tools. In the current study the secondary flow through the compressor disk cavities is simulated using Computational Fluid Dynamics (CFD) and the results are analysed and reported. The analysis of these results help in a better understanding of the distribution of the flow and the variations of the thermal fluid parameters across the secondary flow system. These results are also later used as thermal boundary conditions in the Finite Element model (FEM) to study the impact of various engine design parameters on the disk temperature gradients after being validated by the experimental results. The findings from this computer aided investigation offers support in make design improvements aimed at lowering the disk temperature gradients and enhancing their useful field life

Keywords: Compressor Secondary Flow, Computational Fluid Dynamics, Aircraft Engine, Compressor Disks, Thermo-fluid analysis.

Nomenclature

T: Temperature, C
ΔT: Temperature difference, K
V: Flow velocity, m s^{-1}
d: Annulus Gap, m
d_h : Hydraulic diameter = 2d, m
ν: Kinematic viscosity of the fluid, m^2 s^{-1}
r : Radius from rotor axis, m
ρ: Density of the fluid, kg m^{-3}
μ: Dynamic viscosity of the fluid, N s m^{-2}
K: Thermal conductivity of air, W m^{-1} K^{-1}
K_{disk}: Thermal conductivity of the disk material, W m^{-1} K^{-1}
h: Heat Transfer Coefficient, W m^{-2} K^{-1}
ω : Disk angular velocity, rad s^{-1}
$R_{b:}$ Cavity outer radius, m
R_a: Cavity inner radius, m
β: Volume expansion coefficient of the fluid, K^{-1}
$R_{O,ax}$: Axial Rossby number
Nu: Nusselt Number
Re_{ax}: Axial Reynolds Number
Re_{ω}: Rotational Reynolds's number
Gr: Grashof number
Pr: Prandtl number
s: Axial width of cavity, m
G: Axial gap ratio
x: Axial distance, m
D_s : Shaft diameter, m
$\dot{m}$: Mass flow rate, kg s^{-1}
xk: Ratio of the air to rotor tangential velocities.
q: Heat flux, W m^{-2}

Subscripts:

sh: Shroud
in: Air inlet to cavity
ax: Axial
av: Average
r: At local radius r from axis
o: Outer
i: Inner
cav: Cavity

1. Introduction

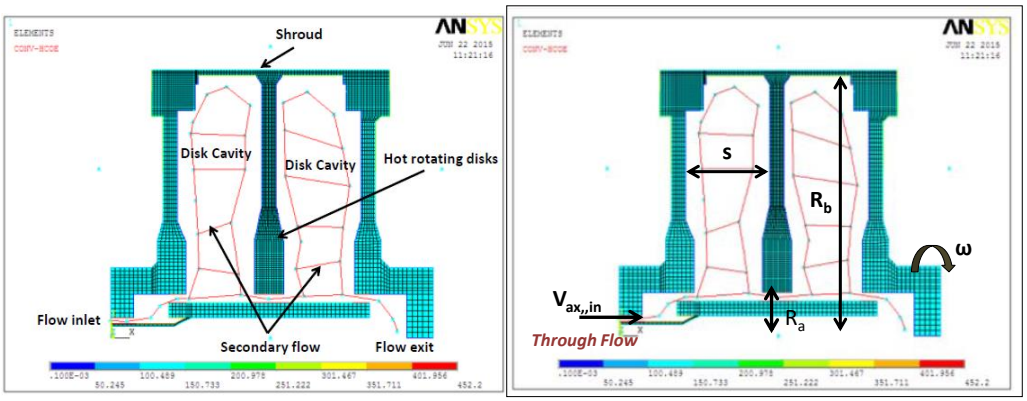

Fig.1 The rotating disks and secondary flow Fig.2 The disk nomenclature

Figure 1 is a schematic of the secondary air flow through the rotating disk cavities. As seen a certain percentage of the secondary through flow circulates into the rotating disk cavities. The amount of this flow re circulation inside the disk cavity depends on

1) The mass of secondary air flow (Represented in terms of the axial Reynolds number).
$Re_{ax} = V_{ax,in}\, d_h / \nu$, Where d_h , $V_{ax,in}$ are the flow diameter and the flow velocity at the inlet.

2) The rotational speed of the disks (Represented in terms of the rotational Reynolds number).
$Re_{\omega} = \omega\, R_b^2 / \nu$, Where ω and R_b are the rotational speed of the disks and the outer radius of the disk cavity.

3) The Axial Rossby number.
$R_{O,ax} = V_{ax,,in} / \omega\, R_a$, Where R_a is the inner radius of the disk cavity.

4) The axial gap ratio.
$G = s / R_b$, Where s , R_b are the axial width and the inner radius of the disk cavity.

The flow simulations are performed using Computational Fluid Dynamics (*CFD*) consistent with the experimental set up (Figure 4) conducted by A. Gunther, L. Heller [5]. The simulations are performed for the two operating conditions of the engine as shown in table 1. Lower operating condition where the secondary mass flow is 0.04 Kg/sec with an engine rotational speed of 6000 r.p.m. Higher operating condition where the secondary mass flow is 0.4 Kg/sec with an engine rotational speed of 12000 r.p.m.

Table 1 shows the details of the two operating conditions of the engine which are modelled and analysed.

Table .1 The two operating conditions of the engine

	ΔT	**Re_{ax}**	**Re_{ω}**	**Gr**	**$R_{O,ax}$**	**$\dot{m}$**	**N**
	K					kg/s	r.p.m
Measurement Test conditions	70	2×10^4	1.5×10^6	6×10^{11}	1	0.04	6000
Maximum test conditions	70	1.8×10^5	1.5×10^7	5×10^{13}	1	0.4	12000

The change in the engine operating condition impacts the thermo-fluid factors listed below 1,2,3 which ultimately influence the heat transfer phenomenon occurring inside the rotating disk cavities. The *CFD* simulation is performed to estimate these thermo-fluid parameters related to the secondary flow system which are later used as boundary conditions in the Finite Element Model (*FEM*) to predict the disk temperature gradients.

1) Pressure, Temperature and density variations of the flow inside the disk cavities.
2) Swirl velocities of re circulating flows inside the disk cavities.
3) The flow structure and the flow distribution within the disk cavities.

2. The CFD Simulation:

The following are some of the earlier studies carried out related to the flow in a rotating cavity similar to that of the rotating compressor disk using computational fluid dynamics (*CFD*). Tucker P.G, Long C.A [1] had conducted a *CFD* study to investigate the vortex flow in a rotating cavity with an axial through flow of air. K. Saunders, S. Alizadeh [2] used the *CFD* study to Generate Heat Transfer Boundary Conditions for a Rotor-Stator Cavity. J. Michael Owen, Hans Abrahamsson [3] had carried out a *CFD* study to study the Buoyancy-Induced Flow in Open Rotating Cavities. Daniele Massini, Bruno Facchini [4] carried out an investigation on Swirl and Heat Transfer Within a Rotor-Stator Cavity.

In the current study the secondary flow simulation is performed using Computational Fluid Dynamics (*CFD*) consistent with the experimental set up (Figure 4) conducted by A. Gunther, L. Heller [5] for the two operating conditions listed in table 1.The *CFD* model is constructed using commercially available Gambit and Fluent software. Figure 3 represents the CFD model and Figure 4 represents the experimental set up

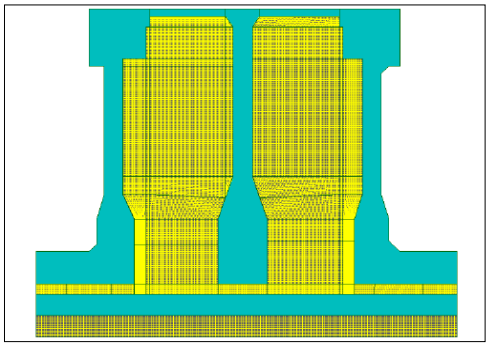

Fig. 3 The CFD model

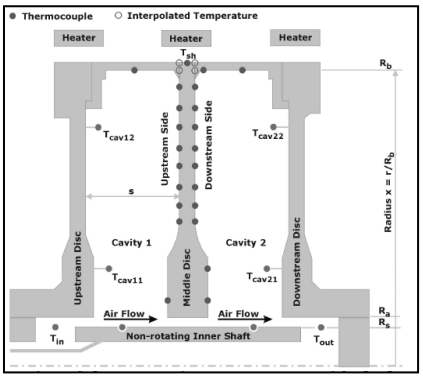

Fig. 4. The experimental set up

The model is a 2D axi-symmetric model with the flow domain meshed with the Quad elements using the Map scheme. The mesh consists of 32330 quadrilateral cells and 33156 nodes. The boundary zone types applied along the flow domain are fixed and rotating walls, mass flow inlet, pressure outlet and axis of rotation (figure 6). The boundary conditions as applied in the Fluent model are shown in figures 5 and 6.

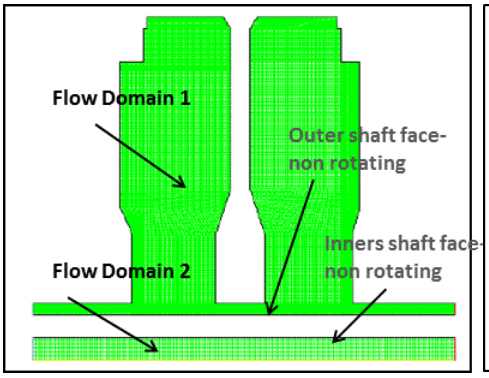

Fig. 5. Fluent Boundary Conditions

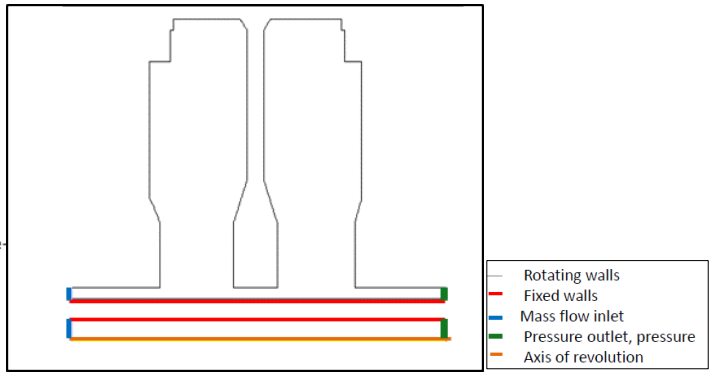

Fig. 6. Fluent Boundary Conditions

The flow model in Fluent model is also 2D axi-symmetric modelled using a Swirl Segregated solver. It has the following modelling features.

1. Compressible flow with application of the energy equation.
2. Uses Spalart-Allmaras 1 equation model for the viscous flow solution.
3. The effects of gravity and buoyancy are captured.
4. Flow domain is air with air with the standard properties.

The flow domain is solved using the flow, the swirl velocity, the modified turbulent viscosity and the energy differential equations with the first order discretization.

3. Results and Discussions:

3.1. The Secondary Flow Pattern and Distribution :

Based on the flow vector patterns obtained from Fluent analysis (Figure 5) , the flow distribution inside the cavities was

estimated and was later used to construct the flow network in the FEA model (figure 6). As observed from the flow vectors in

Fluent, the flow moves radially upwards (up wash) towards the left of the cavity and then radially downwards (down wash)

towards the right of the cavity with internal re circulations from the right to the left of cavity (cross flow). An estimated 20

percent of the incoming flow circulates into the inter disk cavity with 2 percent local re circulations (figure 7). For the measured

test conditions, 100 percent incoming flow (figure 7) corresponds to 0.04 Kgs / sec and for maximum test rig conditions

corresponds to 0.4 Kgs / sec.

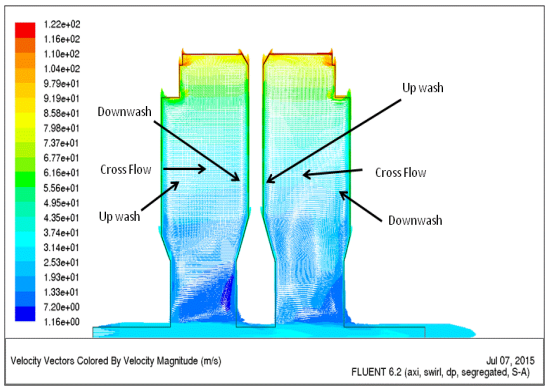

Fig. 5. Flow vector pattern in Fluent

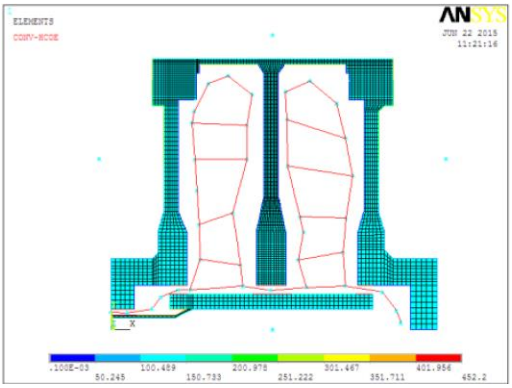

Fig. 6. The flow circulation pattern

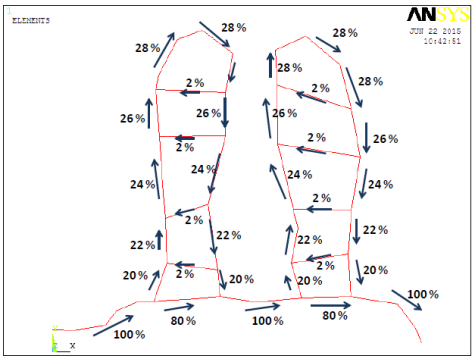

Fig. 7. Estimated percentage of flow re circulation

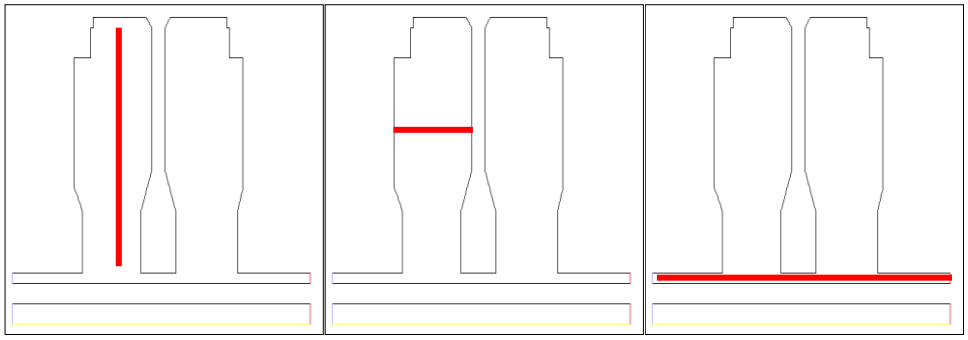

Fig. 8. Location of plotted results Fig. 9. Location of plotted results Fig. 10. Location of plotted results along the cavity radius across the cavity width along the through flow

3.2 The Flow Pressure Variations:

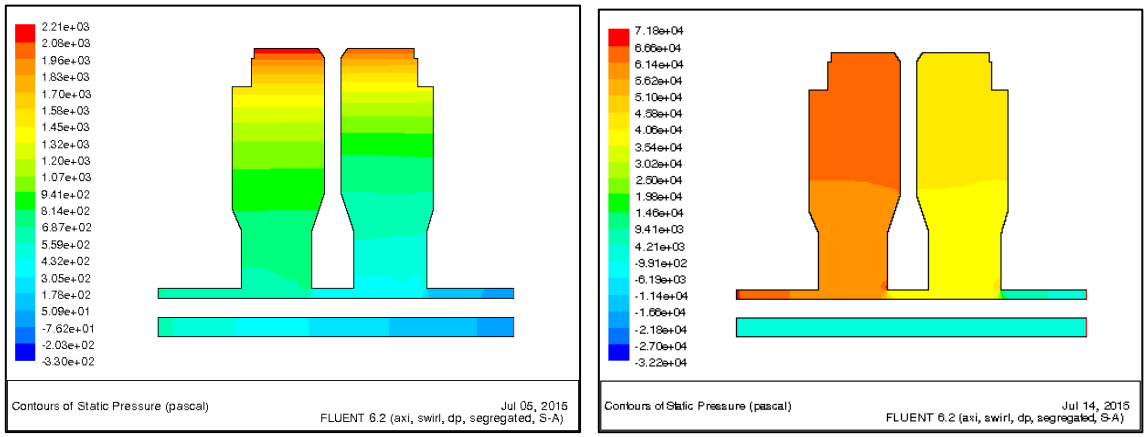

Fig. 11. Pressure variations contours for measured test conditions Fig. 12. Pressure variations contours for max test conditions

Figures 11 and 12 represent the pressure contours obtained for the two engine operating conditions listed in table 1. Figures 13 and 14 show the pressure variations along the radius of the cavity (figure 8) for these two operating conditions. The horizontal scale in these figures represents the radial location in the cavity from the axis of rotation. The results tabulated in table 2 indicate the percentage increase of flow pressures from the inner to the outer radius of the cavity for the two engine operating conditions.

For the test and measurement conditions, as seen from the results (figure 11,13) and the tabulated results (table 2) the pressure build up from the *inner to the middle* radii of the cavity is steady and gradual. The pressure rise at the inner radius is 14 percent compared to 71 percent at the middle radius of the cavity (table 2). But from the *middle to the outer* cavity radius there is a significant pressure build up from 71 to the percent 214 percent (table 2). This phenomenon of higher pressure gradients occurring towards the outer radii is due to the closer interaction of the flow with the rotating shroud and the higher tangential speeds of the rotor towards the outer radii.

For the maximum test conditions, as seen from the results (figure 12,14) and the tabulated results (table 2) the pressure build up throughout from the inner to the outer radii of the cavity is steady and gradual. The

uniformity of pressure gradients throughout the cavity is due to higher mass of the through flow getting ingested into the cavity for the maximum test condition. The higher mass of flow in the cavity reduces the impact of the rotating shroud and the disk over the pressure build up and make the pressure rise more gradual and uniform.

Also as observed from the results (figures 13, 14, table 2) the percentage rise in pressure along the cavity radius for the maximum condition is significantly low compared to the test condition. At the middle of the cavity for the maximum condition the pressure rise is only 3 percent compared to 71 percent for the test condition. This brings to light an important finding of this investigation that the impact of the rotating disks on the pressure gradients significantly reduces with the increase of the mass of air that gets ingested into the rotor cavity. Or in simpler terms the rotational speed of the rotor has a greater impact on the pressure changes with a lower mass of air ingestion into the rotor cavity.

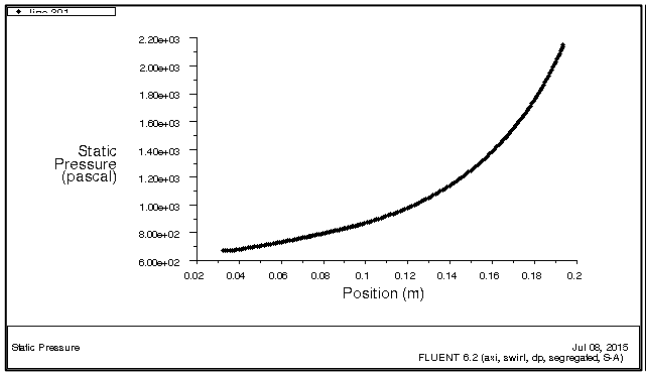

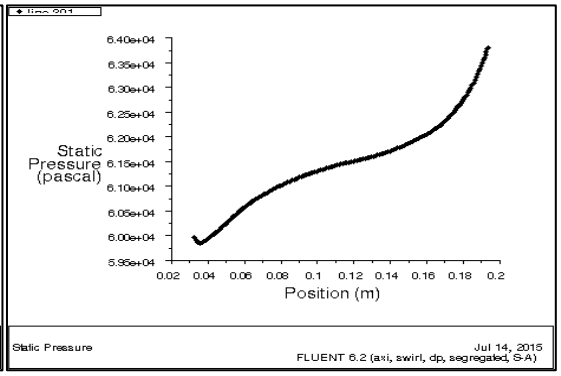

Fig.13. Pressure variation along the cavity radius for measured conditions Fig.14. Pressure variation along the cavity radius for max conditions

Table .2 Air pressure variations along the cavity radius for the two operating conditions

	Percent increase in pressure	
Air Cavity Location	Test Condition	Maximum Condition
Inner Cavity Radius	14	2
Middle Cavity Radius	71	3
Outer Cavity Radius	214	7

Figures 15 and 16 show the pressure variations across the width of the cavity (figure 9) for the two operating conditions (table 1). The horizontal scale in these figures represents the axial location across the cavity width. As observed from these figures the pressure increases continuously across the width from the right to the left rotating wall of the cavity. This rise in pressure towards the left wall of the cavity is due to the flow accumulation towards the left wall on account of the cross flow coming from the right wall (figures 5,7). Also as observed from the results of the test conditions (figure 15) the pressure rise across the cavity width is by 1 percent compared to the maximum condition (figure 16) where the pressure rise is by 6 percent. This higher percentage increase in the pressures across the cavity for the maximum condition is

on account of higher mass of the cross flow that mergers with the outward flow adjacent to the left rotating wall (figure 7).

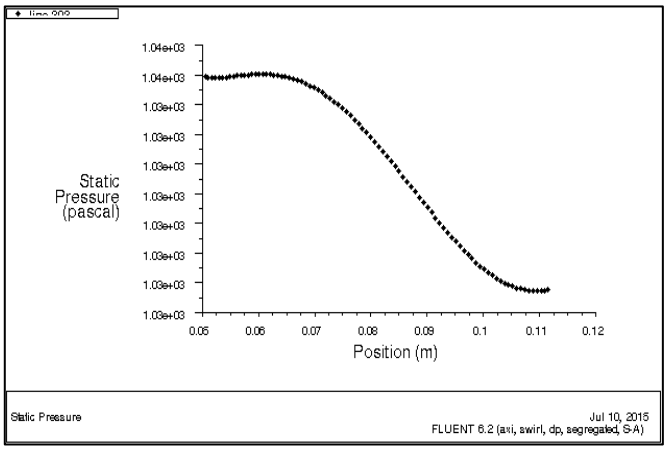

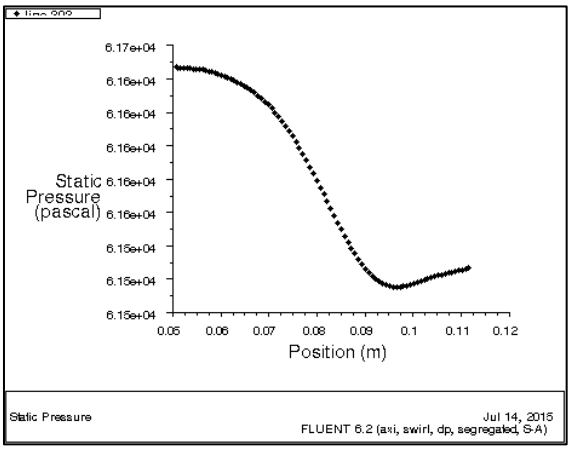

Fig.15. Pressure variation along the cavity width for measured conditions Fig.16. Pressure variation along the cavity width for max conditions

Figures 17 and 18 show the pressure variations along the through flow from the inlet to the exit (figure 10) for the two operating conditions (table 1). The horizontal scale in these figures represents the axial location of the through flow. As observed from these results (figures 17,18) there is a continuous decrease in pressure from the inlet to the exit of the through flow but with a sudden rise in pressure at two locations where the through flow crosses the bottom of the two rotor cavities. For the test condition the rise in this pressure across the cavity is 16 percent compared to 13 percent for the maximum condition. The higher percentage of the pressure rise for the minimum condition is due to the greater impact of the rotating disk over through flow crossing the cavity with lower mass and lower velocities compared to that of the maximum condition.

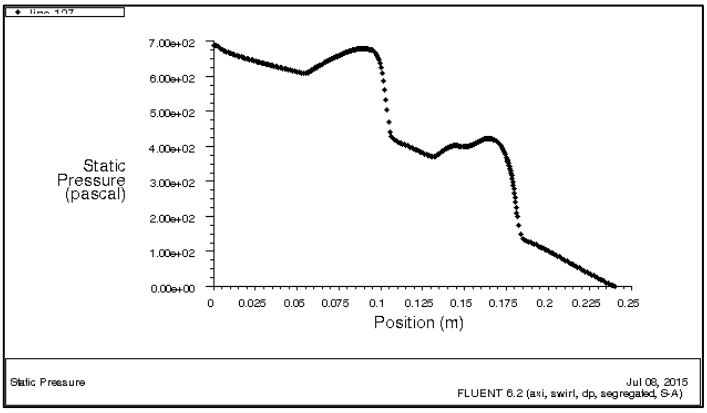

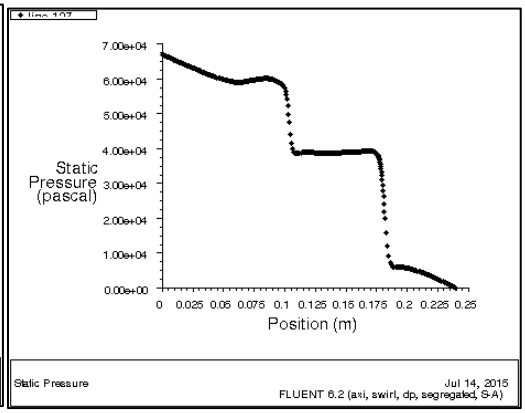

Fig.17. Pressure variation along through flow for measured conditions Fig.18. Pressure variation along through flow for max conditions

3.3. The Swirl Velocity Variations:

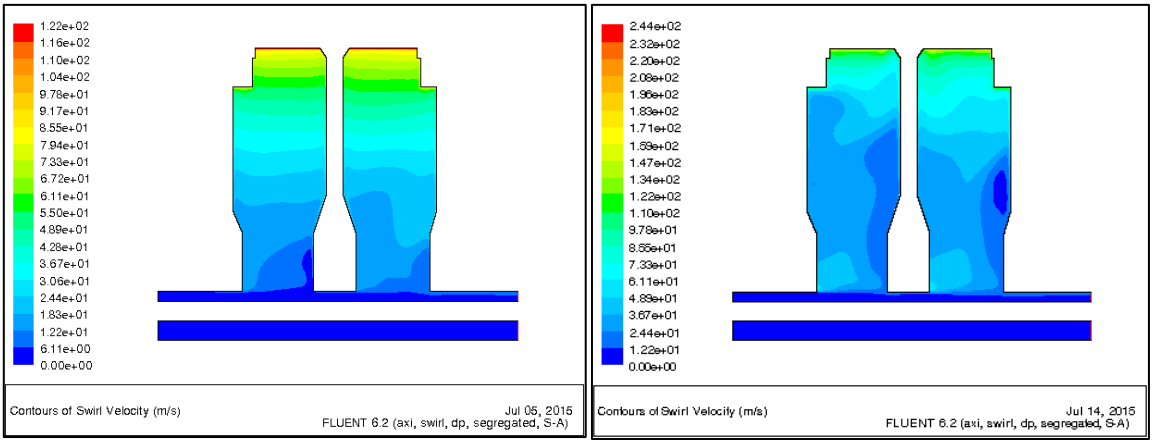

Fig. 19. Swirl velocity contours for measured test conditions Fig. 20. Swirl velocity contours for max test conditions

Figures 19 and 20 represent the swirl velocity contours obtained for the two operating conditions listed in table 1. For the measured test conditions as observed from the swirl velocity contours (figure 19), the increase in the swirl velocity from the inner to the outer radius of the cavity is more steady and gradual. On the contrary for the maximum test conditions (figure 20) the increase in the swirl velocity from the inner to the outer radius is rather unsteady and this increase is much more rapid towards the outer radii near the shroud region.

Figures 21 and 22 show the swirl velocity variations along the radius of the cavity (figure 8) for the two operating conditions (table 1).. The horizontal scale in these figures represents the radial location in the cavity from the axis of rotation. For the test and measurement conditions (figure 21) the increase in the swirl velocity from the inner to the outer radius is steady, gradual and more linear in nature. On the contrary for the maximum test conditions (figure 22) rate of increase in the swirl velocity is more unsteady and non linear. Also as noticed for the maximum condition (figure 22) towards the inner radius of the cavity there is a very minimum increase in the swirl velocity but towards the outer regions near the shroud the rate of increase is significantly higher. This phenomenon of relatively lower rate of increase in swirl velocity at lower radii for the maximum conditions compared to the measured test conditions is attributed to the relative effects of the through flow and the rotating disks over the cavity flow. For the test measurement conditions (figure 21) due to the smaller mass of air, the effect of the rotating disk on the cavity flow is more dominant than the through flow. Hence the increase in the swirl velocities from the inner to the outer radii is steady and consistent. On the contrary for the maximum test conditions (figure 22) due to higher mass of air the through flow has it's greater influence into the lower radial regions of the cavity. Hence the increase in the swirl velocity is very minimal in the inner regions of the cavity (figure 22) but suddenly picks up in the outer regions towards the shroud because of the more dominant effects of the rotating disks and the rotating shroud. Also as observed from figures 21 and 22, for both the measurement and maximum test conditions the rate of increase in the swirl velocities is higher towards the cavity outer regions which is attributed to the higher tangential speeds of the rotor at larger radii and the additional effect of the rotating shroud over the cavity flow. Another key observation is that in case of the measurement test conditions the swirl velocity increases by about 11 times from the inner to the outer radius compared to 18 times for the

maximum test conditions. Although as expected the increase in the swirl velocity is higher for the maximum conditions but unexpectedly is not as high enough relative to the increase in the disk rotational speeds from the measurement to the maximum condition. This again is due to the fact that for maximum conditions the through flow shows it's greater influence into the cavity and slows down the rate of swirl velocity increase in the inner regions of the cavity.

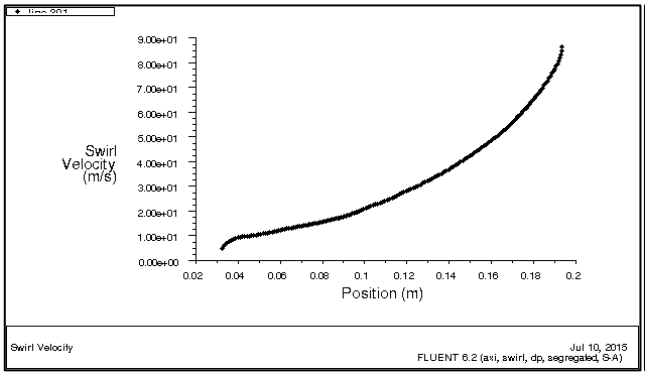

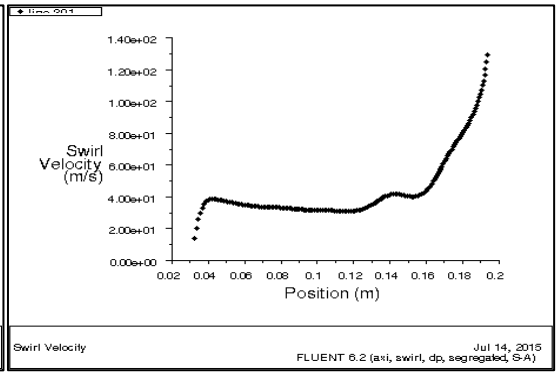

Fig.21.Swirl velocity variation along cavity radius for measured conditions Fig.22. Swirl velocity variation along radius for max conditions

Figures 23 and 24 show the swirl velocity variations across the width of the cavity (figure 9) for the two operating conditions (table 1). The horizontal scale in these figures represents the axial location across the cavity width. For both the measurement conditions (figure 23) and the maximum test conditions (figure 24) the maximum swirl velocities are observed very close to the two rotor walls and is attributed to the viscous effects of the near wall boundary layer. But across the cavity higher swirl velocities are observed closer towards the left rotating wall (figures 23 and 24) and this shift of higher velocities towards the left wall is more noticeable in case of the maximum test conditions (figure 24). This is due to the fact that the cross recirculation of the flow as observed in this study is from the right rotating wall towards the left rotating wall (figure 7). The mass of this recirculating flow merging with the radial outward flow along the left wall (figure 7) results in higher swirl velocities towards the left of the cavity. And this effect is more dominant in case of maximum condition (figure 24) because of higher mass of the recirculating cross flow compared to the test condition.

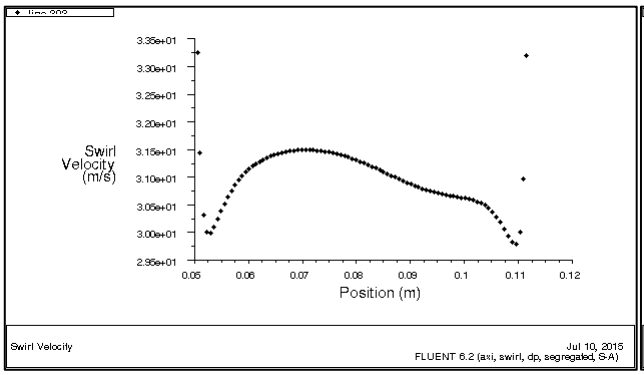

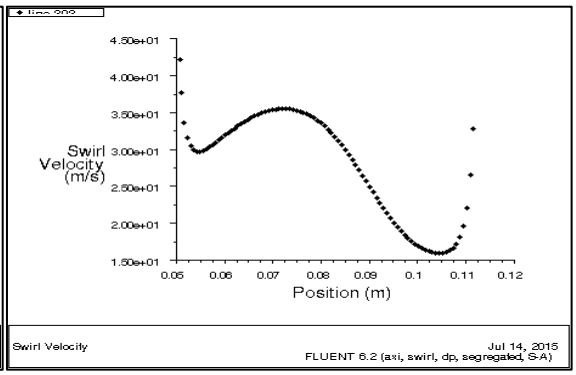

Fig.23. Swirl velocity variation along cavity width for test conditions Fig.24. Swirl velocity variation along cavity width for max conditions

Figures 25 and 26 show the swirl velocity variations along the through flow from the inlet to the exit (figure 10) for the two operating conditions (table 1). The horizontal scale in these figures represents the axial location of the through flow. As observed from these figures, the swirl velocity along the through flow increases from the inlet to the exit. Also as observed from these results (figures 25, 26) the increases in this swirl velocity is experienced only at the regions where the through flow crosses the rotor cavities and this increase is more significant for the maximum test conditions (figure 26). Hence at higher rotational speeds as a greater mass of the through flow gets ingested into the rotor cavities the induced swirl causes a more significant impact over the swirl velocities of the through flow.

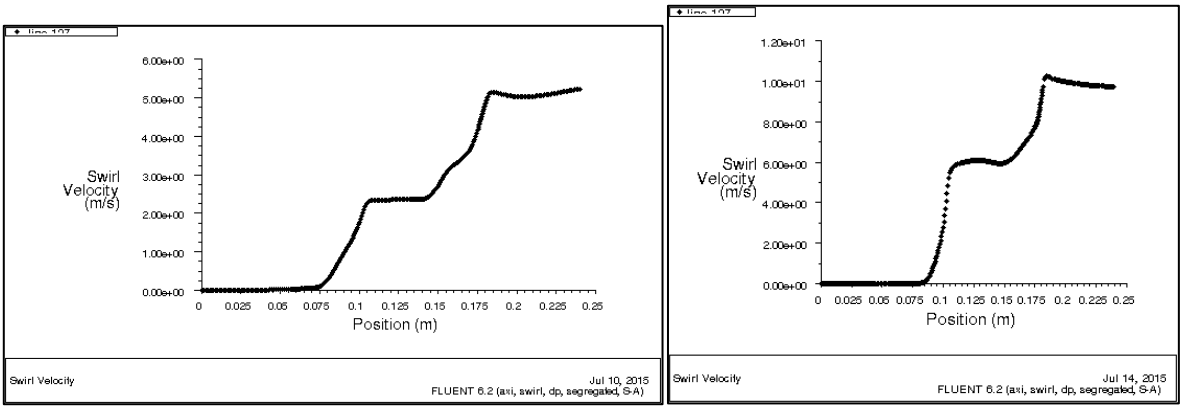

Fig.25. Swirl velocity variation along through flow for test conditions Fig.26. Swirl velocity variation along through flow for max conditions

3.4 The Flow Temperature Variations:

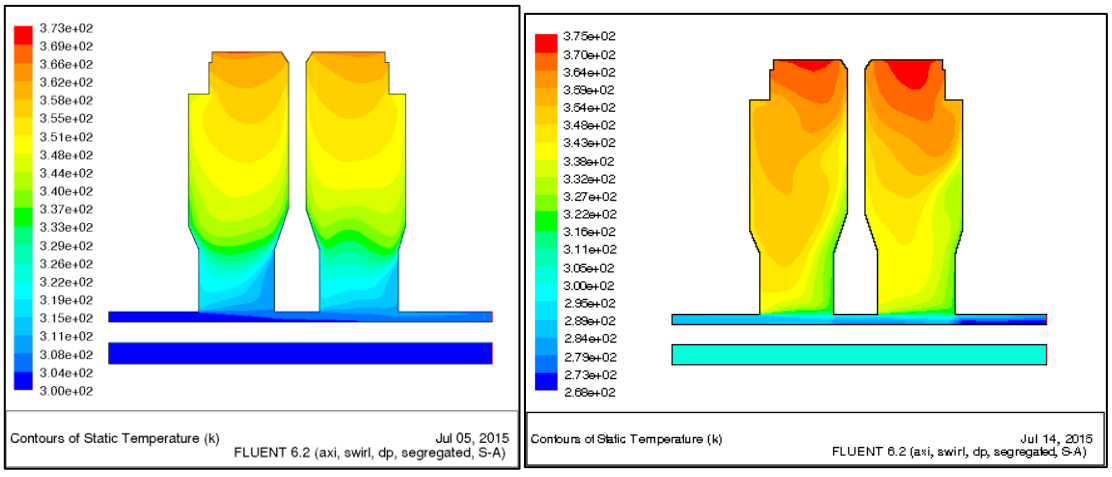

Fig. 27. Air temperature contours for test conditions Fig. 28. Air temperature contours for max conditions

Figures 27 and 28 represent the air temperature contours obtained for the two engine operating conditions listed in table1.

Figures 29 and 30 show the air temperature variations along the radius of the cavity (figure 8) for these operating conditions. The horizontal scale in these figures (29,30) represents the radial location in the cavity from the axis of rotation.

As observed from the temperature contours (figures 27,28) and the plots (figures 29,30) the cavity air temperature rises with the increase in the operating condition of the engine. This rise in the cavity air temperatures for the maximum test conditions is attributed to the increased levels of heat transfer between the hotter rotor and the cooler air caused by higher levels of buoyancy induced flow at higher rotational speeds.

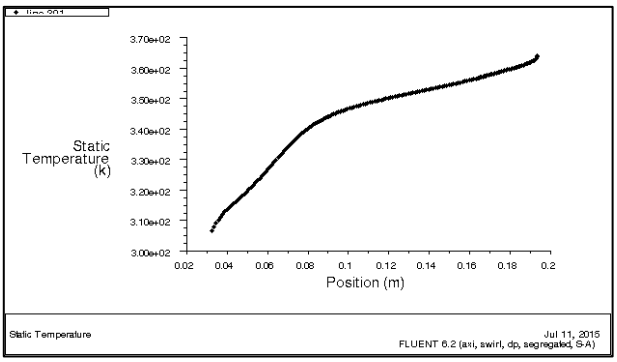

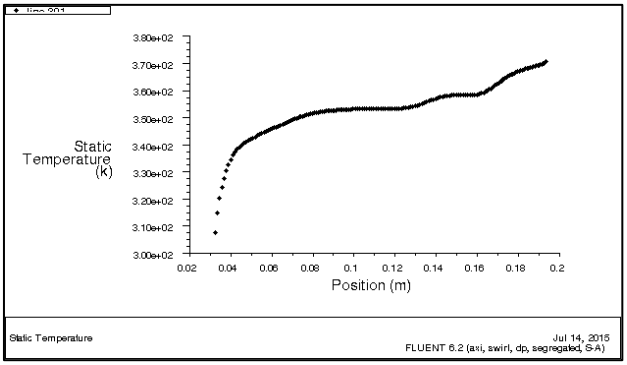

Fig.29. Air temperature variation along cavity radius for test conditions Fig.30. Air temperature variation along cavity radius for max conditions

The results tabulated in table 2 indicate the percentage increase of air temperatures from the inner to the outer radius of the cavity for the two engine operating conditions. As observed (table 2) the impact of changes in the operating condition over the air temperatures is much more significant towards the inner regions of the cavity compared to the outer regions. This is attributed to the fact that at inner radii air is relatively cooler resulting in higher air densities enhancing the levels of buoyancy induced flow caused by the rotational effects of the rotor as compared to the outer radii of the cavity.

Table .2 Air temperature variations along the cavity radius for two operating conditions

Air Cavity Location	*Percent increase in air temperature*	
	Test Condition	Maximum Condition
Inner Cavity Radius	7	17
Middle Cavity Radius	17	22
Outer Cavity Radius	20	24

Figures 31 and 32 show the air temperature variations across the width of the cavity (figure 9) for the two operating conditions (table 1).. The horizontal scale in these figures represents the axial location across the cavity width. As observed from these results (figures 31,32) higher air temperatures are noticed towards the middle portion of the cavity width. This is a result of the higher rates of heat transfer from the rotating shroud which has the maximum temperature. Also as observed, with the increase in the operating condition,

the maximum temperature across the width cavity shifts towards the left rotating wall (figure 32). This is attributed to the fact that at higher operating condition there is an increased mass of cross flow (figure 5,7) from the right rotating wall towards the left rotating wall causing the maximum air temperature to shift towards the left of the cavity width.

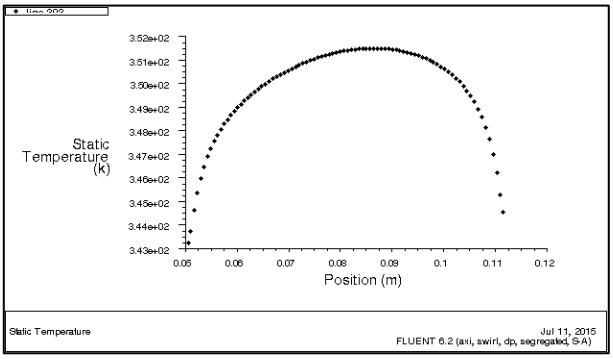

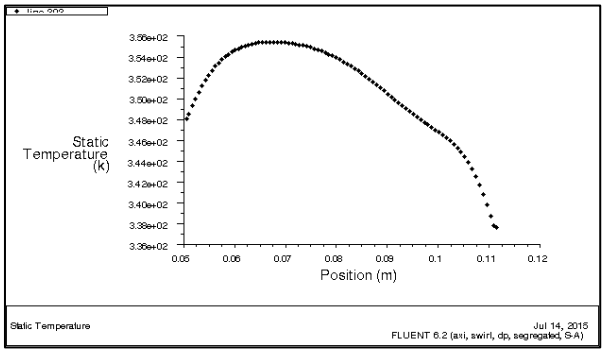

Fig.31. Air temperature variation along cavity width for test conditions Fig.32. Air temperature variation along cavity width for max conditions

3.5 The Flow Density Variations:

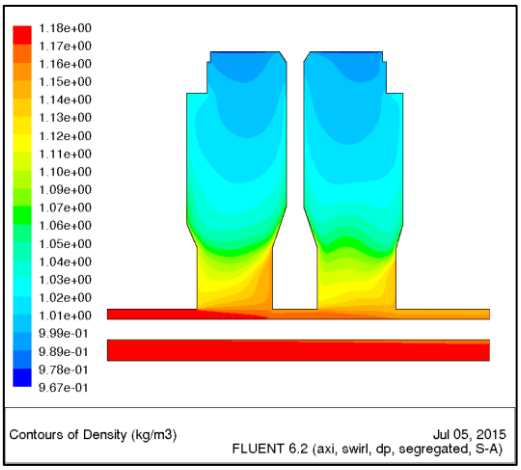

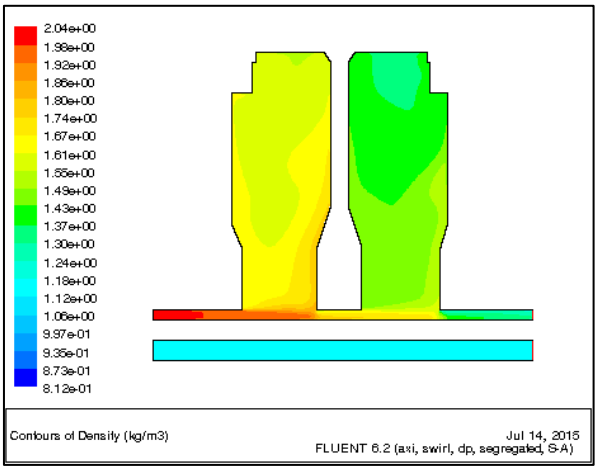

Fig. 33. Air density contours for test conditions Fig. 34. Air density contours for max conditions

Figures 33 and 34 represent the air density contours obtained for the two engine operating conditions listed in table1.

Figures 35 and 36 show the air density variations along the radius of the cavity (figure 8) for these operating conditions. The horizontal scale in these figures (35,36) represents the radial location in the cavity from the axis of rotation.

As observed from the density contours (figures 33,34) and the plots (figures 35,36) the air density inside the cavity rises with the increase in the operating condition of the engine. This rise in the air density for the

maximum test conditions is attributed to the increased mass of the through flow which is ingested into the cavity at higher rotational speeds.

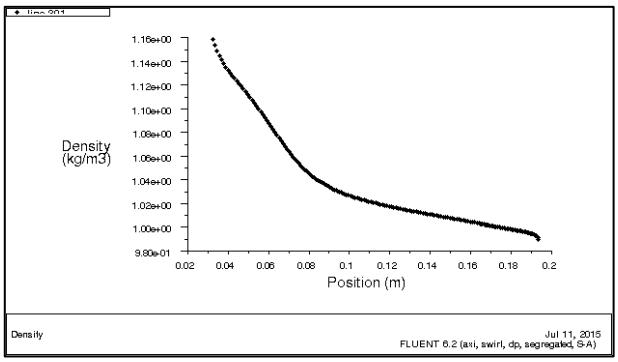

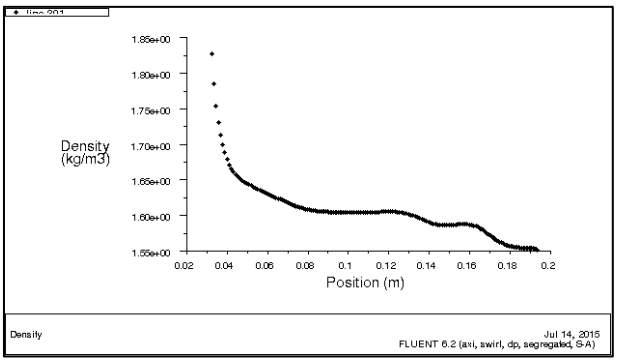

Fig.35. Air density variation along cavity radius for test conditions Fig.36. Air density variation along cavity radius for max conditions

The results tabulated in table 3 indicate the percentage decrease of air density from the inner to the outer radius of the cavity for the two engine operating conditions. As observed (table 3) the impact of the changes in operating condition over the air densities is more significant towards the inner regions of the cavity compared to the outer regions. This is attributed to the fact that at higher operating conditions, the mass of the through flow is higher which results in a more rapid decrease in air density as the air gets initially ingested into the cavity at the inner radii.

Table .3 Air density variations along the cavity radius for two operating conditions

	Percent decrease in density	
Air Cavity Location	Test Condition	Maximum Condition
Inner Cavity Radius	5	10
Middle Cavity Radius	10	12
Outer Cavity Radius	14	16

Figures 37 and 38 show the air density variations along the through flow from the inlet to the exit (figure 10) for the two operating conditions (table 1). The horizontal scale in these figures represents the axial location of the through flow. As observed from these figures, the air density along the through flow decreases from the inlet to the exit on account of the pressure differential maintained across the rotor. As observed from the results (figures 37,38) most of the pressure drop occurs in the regions of the through flow where the flow gets ingested into the rotor cavities. For the maximum condition (figure 38) the drop in pressure of the through flow across the cavity is 10 percent compared to only 2 percent for the test condition (figure 37). This shows that higher rotational speeds of the rotor show a significant impact on the pressure drop that occurs in through flow as it moves across these rotor cavities.

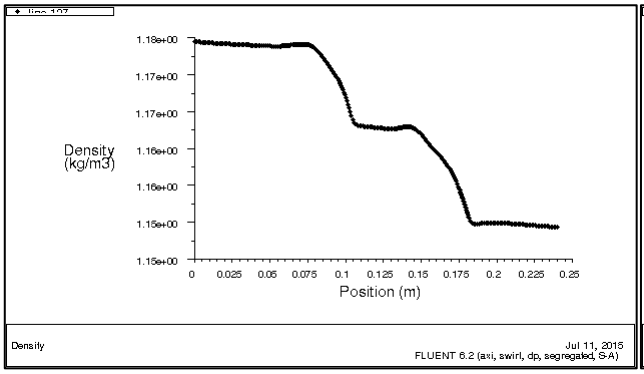

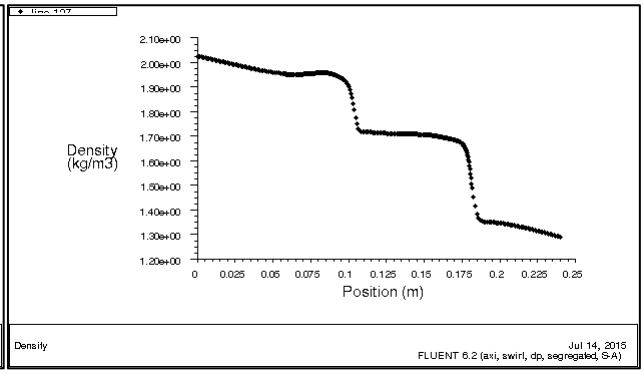

Fig.37. Density variation along through for test conditions Fig.38. Density variation along through for max conditions

4. Estimation of heat transfer coefficients and model validation with experimental results:

The convective heat transfer coefficients in the various regions of the rotor interacting with the secondary flow are estimated based on the correlations developed from the earlier experimental works. In the current study these heat transfer coefficients are estimated for the two engine operating conditions listed in table 1. The estimation of the heat transfer coefficients inside the rotating cavity (vertical faces of the disk) is based on the correlation developed from the experimental work done by Farthing et al. [10,13]. The equation represents laminar natural convection over a vertical plate. The heat transfer in the shroud region of the rotor is modeled as heat flow over a horizontal plate with the upper surface heated and the lower surface exposed to free convection with the effects of gravitation forces captured. The heat transfer correlation used for this case is based on the experimental work carried out by Lloyd and Moran [23]. The heat transfer over the exterior of the disks is modelled as a rotating disk in quiescent air. The correlation is selected based on the experimental work done by S. Harmand, J. Pelle [8] which involves a rotating disk in quiescent air. The heat transfer inside the annulus between the rotating disk and the shaft is modelled as an annulus flow and the correlation is based on the experimental studies carried out by S. Seghir-Ouali [6]. The heat transfer coefficients estimated from this correlation were checked against the experimental curves obtained by Gazley [12] who used data from an experimental set up with a long rotating cylinder inside a concentric stationary cylinder. The heat transfer over the outer face of the non-rotating shaft is modelled as an axial flow over a cylinder using the correlation developed by the experimental work carried out by Roland Wiberg [14]. The heat transfer phenomenon inside the non-rotating shaft is modelled as an internal duct flow using the standard correlation published in the Heat and Mass Transfer Data book [11].

The thermal boundary conditions estimated from the computational study were later applied in the *Ansys* (*FEM*) model to obtain the temperature distributions over the rotating compressor disks. The *Ansys* model with the applied thermal boundary conditions was validated against the experimental results available for the "test and measurement conditions" from the experimental work done by A. Gunther L. Heller [5]. The validation was done with the radial heat flux data available from the experimental results as shown in figure 40.

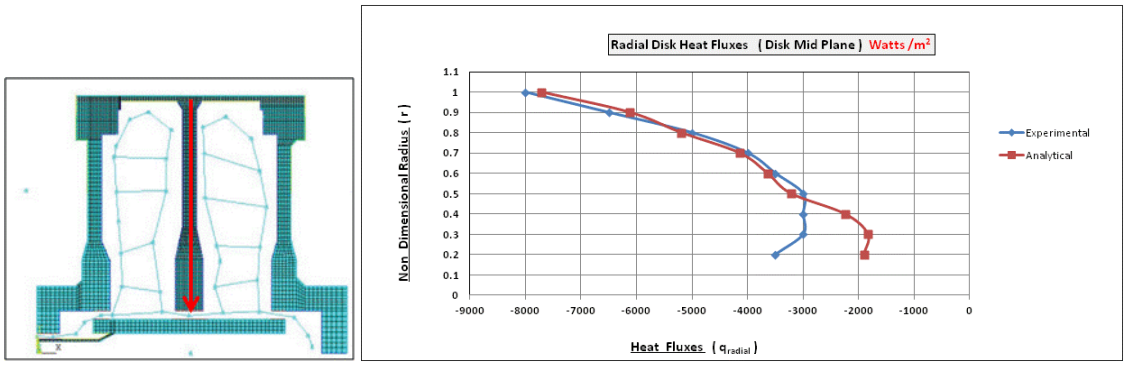

Fig.39 Region where radial heat fluxes are compared Fig.40. Comparison of radial heat fluxes of the analytical model with the experiment

As observed from the compared results in figure 40, the radial heat fluxes estimated using the computational model are in good agreement with the experimental results (within 10 per cent) with the exception of the very lower regions of the rotating disk. The deviation here is due to the sudden change in the thickness of the disk which gives a measurement error as quoted in the experimental work done by A. Gunther L. Heller [5].

5. Conclusions:

The design of the secondary flow system in an aircraft engine is vital in terms of lowering the temperature gradients experienced by the rotating compressor disks to enhance their field life. As it is almost impractical to conduct experiments for the large number of secondary flow design parameters and the range of engine operating conditions it becomes inevitable to build a computational model that closely simulates the thermal behaviour of the secondary flow system. In this study the secondary flow simulation is carried out using computational fluid dynamics (*CFD*) and the computer model used for these simulations is validated against the available experimental data.

During this study carried out using computational fluid dynamics *(CFD)* the distribution of the various thermal fluid parameters namely the flows, the velocities, the temperatures, the densities across the secondary flow system is investigated for the two operating conditions of the engine (table 1). These thermal fluid parameters are later used as boundary conditions in the Finite Element Model (*FEM*) to study the thermal impact of the engine design parameters and the engine operating conditions on the disk temperature gradients. The results obtained from the current *CFD* analysis are analysed and the important findings of the investigation are reported. The findings coming out of this investigation help in a better understanding of the complex thermal phenomenon occurring inside the secondary flow system and offers support in making secondary flow design improvements aimed at lowering the disk temperature gradients.

Acknowledgments

I would like to acknowledge the necessary support provided by the C.B.I.T and the Osmania University for the successful execution and completion of this research work

References

[1] TuckerP.G, Long C.A. (1995), CFD prediction of vortex breakdown in a rotating cavity with an axial through low of air, International Communications in Heat and Mass Transfer, Volume 22, Issue 5, September–October 1995, Pages 639-648

[2] K. Saunders, S. Alizadeh, (2007), The Use of CFD to Generate Heat Transfer Boundary Conditions for a Rotor-Stator Cavity in a Compressor Drum Thermal Model, ASME Turbo Expo 2007: Volume 4 : Turbo Expo 2007, Parts A and B
Montreal, Canada, May 14–17, 2007

[3] J. Michael Owen, Hans Abrahamsson, (2007), Buoyancy-Induced Flow in Open Rotating Cavities, J. Eng. Gas Turbines Power 129(4), 893-900 (Jan 11, 2007).

[4] Daniele Massini, Bruno Facchini, (2016), Experimental Investigation on Swirl and Heat Transfer Within a Rotor-Stator Cavity, ASME Turbo Expo 2016: Turbomachinery Technical Conference and Exposition, Volume 5A: Heat Transfer
Seoul, South Korea, June 13–17, 2016

[5] A. Günther, W. Uffrecht, L. Heller, S. Odenbach (2009), Experimental and Numerical Analysis of Heat Transfer in Compressor Disc Cavities for a transition between Heating and cooling flow. 8th ETC, Graz, 111

[6] S. Seghir-Ouali a, (2006), Convective heat transfer inside a rotating cylinder with an axial air flow, International Journal of Thermal Sciences 45 (2006) 1166–1178.

[7] Sparrow, E. M., and Leonardo Goldstein Jr., (1976), Effect of rotation and coolant through flow on the heat transfer and temperature field in an enclosure, J. Heat Transfer, 98, pp. 387-394.

[8] S. Harmand, J. Pelle, S. Poncet , I.V. Shevchuk (2013), Review of fluid flow and convective heat transfer within rotating disk cavities with impinging jet, International Journal of Thermal Sciences, volume 67 (2013) , 1-30

[9] Owen, J. M., and Pincombe, J. R., 1979, “Vortex Breakdown in a Rotating Cylindrical Cavity,” J. Fluid Mech., 90, pp. 109–127

[10] Farthing, P. R., Long, C. A., Owen, J. M., and Pincombe, J. R., (1992), Rotating Cavity With Axial Through flow of Cooling Air: Heat Transfer, J. Turbomach., 114, pp. 229–236

[11] CP Kothandaraman , S Subramanyan, Heat and mass transfer data book, 116-117, Fourth edition, New age international publishers.

[12] C. Gazley, Jr., (1958), Heat transfer characteristics of the rotation and axial flow between concentric cylinders,
ASME Trans. 80,79-90

[13] Farthing, P. R., Long, C. A., Owen, J. M., and Pincombe, J. R., (1992), Rotating Cavity with Axial Through flow of Cooling Air: Flow Structure, ASME J. Turbomach., 114, pp. 237–246.

[14] Roland Wiberg , Noam Lior, (2005), Heat transfer from a cylinder in axial turbulent flows, International Journal of Heat and Mass Transfer 48 (2005) 1505–1517.

[15] X. Luo, L. Wang, X. Zhao, G. Xu, H. Wu, (2014), Experimental investigation of heat transfer in a rotor–stator cavity with cooling air inlet at low radius, International Journal of Heat and Mass Transfer, Volume 76, September 2014, Pages 65-80

[16] Dr. K.E. Reby Roy and K. Madhusoodanan Pillai, Flow and Conjugate Heat Transfer Characteristics in a Rotating Disk Cavity with through-Flow, International Journal of Applied Engineering Research, Volume 7, Number 12 (2012) pp. 1429-1441.

[17] Sparrow, E. M., Buszkiewicz, T. C., and Eckert, E. R. G., 1975, “Heat transfer and temperature field experiments in a cavity with rotation, recirculation and coolant through flow,” J. Heat Transfer, 97, pp. 22-28.

[18] Xiang Luo, L. Wang, (2014), Experimental investigation of heat transfer in a rotor–stator cavity with cooling air inlet at low radius, International Journal of Heat and Mass Transfer 76:65–80.

[19] J. Michael Owen, Jonathan Powell, Buoyancy-Induced Flow in a Heated Rotating Cavity, Transactions of the ASME, Vol. 128, January 2006.

[20] C. A. Long and P. G. Tucker, Shroud Heat Transfer Measurements From a Rotating Cavity With an Axial Through flow of Air, J. Turbomach 116(3), 525-534.

[21] C. A. Long, Disk heat transfer in a rotating cavity with an axial through flow of cooling air, Int. J. Heat and Fluid Flow, Vol. 15, No. 4, August 1994

[22] Dayle C. Jogie, (2016), The study of fluid flow and heat transfer of a viscous incompressible fluid between a rotating solid disk and a stationary permeable disk using the Brinkman-Darcy model, Journal of Applied Mathematics and Mechanics, 96:5, 620-632

[23] Lloyd, J.R., Moran, W.R., (1974)., Natural convection adjacent to horizontal surfaces of various planforms", ASME Paper 74-WA/HT- 66.

[24] M.M. Rahman, J.C. Lallave, A. Kumar, (2008), Heat Transfer from a Spinning Disk during Semi–Confined Axial Impingement from a Rotating Nozzle, Int. J. Heat Mass Transfer 51, 4400–4414.

[25] D.A. Howey a, A.S. Holmes a , K.R. Pullen b, (2010), Radially resolved measurement of stator heat transfer in a rotor–stator disc system, International Journal of Heat and Mass Transfer 53, 491–501

[26] R. P. Roy, G. Xu and J. Feng, (2001), A Study of Convective Heat Transfer in a Model Rotor–Stator Disk Cavity, J. Turbomach 123(3), 621-632